Single Particle Image Reconstruction of the Human Recombinant Kv2.1 Channel

Brian Adair,* Rashmi Nunn,* Shannon Lewis,* Iain Dukes,† Louis Philipson,‡ and Mark Yeager*§¶

*The Scripps Research Institute, Department of Cell Biology, La Jolla, California 92037; †Glaxo Wellcome Research Institute, Department of Molecular Endocrinology, Research Triangle Park, North Carolina 27709; ‡University of Chicago, Department of Medicine, Section of Endocrinology, Chicago, Illinois 60637; §Division of Cardiovascular Diseases, Scripps Clinic, La Jolla, California, 92037; and ¶Department of Molecular Physiology and Biological Physics, University of Virginia Health Sciences Center, Charlottesville, Virginia

ABSTRACT Kv2.1 channels are widely expressed in neuronal and endocrine cells and generate slowly activating K^+ currents, which contribute to repolarization in these cells. Kv2.1 is expressed at high levels in the mammalian brain and is a major component of the delayed rectifier current in the hippocampus. In addition, Kv2.1 channels have been implicated in the regulation of membrane repolarization, cytoplasmic calcium levels, and insulin secretion in pancreatic β-cells. They are therefore an important drug target for the treatment of Type II diabetes mellitus. We used electron microscopy and single particle image analysis to derive a three-dimensional density map of recombinant human Kv2.1. The tetrameric channel is egg-shaped with a diameter of ~80 Å and a long axis of ~120 Å. Comparison to known crystal structures of homologous domains allowed us to infer the location of the cytoplasmic and transmembrane assemblies. There is a very good fit of the Kv1.2 crystal structure to the assigned transmembrane assembly of Kv2.1. In other low-resolution maps of K^+ channels, the cytoplasmic N-terminal and transmembrane domains form separate rings of density. In contrast, Kv2.1 displays contiguous density that connects the rings, such that there are no large windows between the channel interior and the cytoplasmic space. The crystal structure of KcsA is thought to be in a closed conformation, and the good fit of the KcsA crystal structure to the Kv2.1 map suggests that our preparations of Kv2.1 may also represent a closed conformation. Substantial cytoplasmic density is closely associated with the T1 tetramerization domain and is ascribed to the ~184 kDa C-terminal regulatory domains within each tetramer.

INTRODUCTION

Voltage-gated potassium channels play a vital role in the generation of electrical signals in excitable cells. These channels open in response to voltage changes produced by the previous opening of sodium channels. Voltage-gated potassium channels are typically comprised of four subunits each containing six membrane-spanning sequences (S1–S6) (Fig. 1), with the N- and C-termini on the cytoplasmic side of the membrane (reviewed in Minor (1) and Yellen (2)). The pore domain is formed by S5 and S6, and the connecting loop forms a selectivity filter (P) at the narrowest part of the pore. S1–S4 in potassium channels form the voltage sensing domain, with S4 containing multiple positive charges. The organization of these sequences has been shown in structures of a bacterial channel, KcsA (3,4), an archeal channel, KvAP (5), and a recombinant human channel, Kv1.2, (6) determined by x-ray crystallography. KcsA is not voltage-gated and possesses only two transmembrane (TM) helices, corresponding to S5 and S6, whereas KvAP and Kv1.2 are voltage-gated and contain all six TM regions. S5 and S6 are anti-parallel α-helices that display conserved packing in the available crystal structures. However, S6 diverges at a conserved glycine so the course followed by the polypeptide from the selectivity filter to the cytoplasmic side differs. The KvAP structure possesses a surprising orientation of the S3b-S4 assembly, which was roughly parallel with the bilayer. In contrast, all of the transmembrane helices in the Kv1.2 structure are aligned roughly perpendicular to the membrane plane as expected for a membrane embedded conformation. The S3–S4 assembly in Kv1.2 does, however, possess a similar organization as the equivalent assembly in KvAP, and a simple rigid-body movement of the S3–S4 helices in KvAP generates a conformation very similar to Kv1.2 (7). The relative mobility of the S3–S4 α-helices has led to the hypothesis that this assembly might move toward the extracellular side of the membrane, inducing a reorganization of the S4–S5 linker region and leading to a concerted movement of S5 and S6 and hinging of S6 at the conserved glycine (7,8). The model derived from the x-ray structures posits a very large motion of S3–S4 across the bilayer. However, studies using fluorescence resonance energy transfer indicated relatively small movements of S4 on gating (9). This has led to hypotheses wherein activation involves a rotation and perhaps tilting, with minimal translation of S4 (10). The movement of charge in these models is thought to be facilitated by water-filled crevices, which shorten the distance a charged residue must move to reach either the extracellular or cytoplasmic milieu. A large number of experimental results are compatible with this model (10–12).

Members of the Kv1.x-Kv4.x family of potassium channels also have a tetramerization domain (T1) at the N-terminus (Fig. 1), which determines subunit assembly and serves as an attachment point for other proteins such as

Submitted August 7, 2007, and accepted for publication December 11, 2007.

Address reprint requests to M. Yeager, Tel.: 858-784-8584; Fax: 858-784-2504; E-mail: yeager@scripps.edu

Editor: Edward H. Egelman.

0006-3495/08/03/2106/09 $2.00

doi: 10.1529/biophysj.107.118562

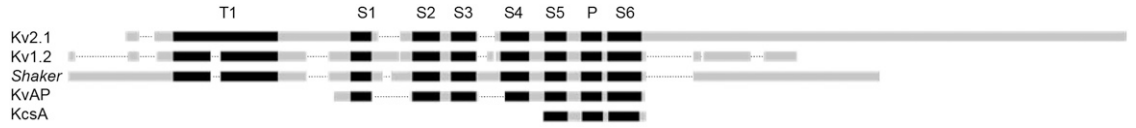

FIGURE 1 Sequence comparisons of voltage gated K^+ channels Kv2.1, Kv1.2, *Shaker*, KvAP, and KcsA. Sequence alignment was carried out with the program Clustal W (44). Protein sequences are indicated by shaded bars. Solid regions delineate the conserved sequences discussed in the text. S1–S6, TM domains; P, selectivity filter. Sequences of human Kv2.1 (NP_004966.1 gi:4826784) and Kv1.2 (P08510 gi:13432103) are from SwissProt.

β-subunits. Indeed, Kv1.2 was crystallized as a complex with an oxido-reductase β-subunit (6). T1 domains form compact tetrameric structures, with the subunits arranged around a narrow pore 20 Å in axial length (13). Three-dimensional (3D) structures of the Shaker K^+ channel (14,15), the Kv1 complex from mammalian brain (16), and recombinant Kv1.2 channels (17) by electron microscopy (EM) and single particle image analysis all show stacked, tetrameric rings in which the smaller tetrameric ring is assigned to the T1 domains. This organization is recapitulated in the x-ray structure of Kv1.2 (6).

Kv2.1 channels are widely expressed in neural and endocrine cells and generate slowly activating K^+ currents that contribute to repolarization in these cells. Kv2.1 channels have both a high voltage threshold for activation and very slow activation kinetics, and are not thought to contribute to the rapidly oscillating depolarization in the action potential (18,19). Instead, sustained Kv2.1 currents seem to regulate the overall action potential by damping and attenuating the voltage oscillations (20). The cytoplasmic domains of Kv2.1 contribute to the channel's activation kinetics. The most striking sequence difference between Kv2.1 and other mammalian Kv channels is that the C-terminal domains of Kv2.1 are substantially larger (Fig. 1), and cytoplasmic amino acids account for 73% of the protein (21). Phosphorylation of the C-terminus can have a dramatic impact on Kv2.1 activation voltage threshold (22). The C-terminal domains contain 15 phosphorylation sites. In vivo, Kv2.1 is phosphorylated at multiple sites, and the effect of phosphorylating these sites is additive (19). The result is a graded regulatory response (19,23). Additional domains within the C- and N-termini have been implicated in the control of channel gating (23–25). The regulation of channel opening requires specific interactions between the C-terminus and the N-terminal T1 domain (24,26). This evidence strongly suggests that the cytoplasmic N- and C-terminal domains are associated in the channel.

Kv2.1 channels have been implicated in the regulation of membrane repolarization, cytoplasmic calcium levels $[Ca^{2+}]_i$, and insulin secretion in pancreatic cells. Pancreatic β-cells depolarize in response to glucose and fire Ca^{2+}-dependent action potentials that trigger insulin secretion. Glucose initiates membrane depolarization by closure of ATP sensitive K^+ channels (27). Membrane depolarization leads to opening of voltage-dependent Ca^{2+} channels that increase $[Ca^{2+}]_i$ to trigger insulin secretion. Membrane repolarization is generated by the delayed rectifier K^+ current. Kv2.1 channels are thought to be the major contributor to the delayed rectifier current in these cells (28). Kv2.1 is expressed in cells purified from rodent pancreatic islets of Langerhans as well as insulinoma cells (29), and the channels are important regulators of insulin secretion (30). Inhibition of Kv2.1 channels can increase glucose-dependent insulin secretion in pancreatic cells (31,32). There is interest in inhibiting Kv2.1 as a therapeutic target (28), because suppression of the delayed rectifier current should broaden the action potential, increasing its strength and duration. Indeed, blockers of Kv2.1 will increase glucose-dependent insulin secretion (33). As a first step to explore the structural basis for these properties of Kv2.1 channels, we determined a 3D structure of Kv2.1 by electron microscopy and single particle image analysis.

MATERIALS AND METHODS

Protein purification

Human Kv2.1 was expressed in a stably transfected line of Chinese hamster ovary (CHO) cells as described previously (29). Cells were isolated by centrifugation and stored at −80°C. The cell pellet (~0.5 g wet weight) was thawed, and the cells were suspended by vortex mixing and solubilized in 1 ml of 25 mM HEPES buffer (pH 7.2) containing 10% sucrose, 1 mM EDTA, and 4.2 mM DHPC (1,2 diheptanoyl-*sn*-glycero-3-phosphocholine) (Avanti Polar Lipids, Birmingham, AL). The cells were maintained at ice temperature and disrupted by sonication (microsonicator, setting 60, 3–4 bursts for a few seconds). Insoluble material was then removed by ultracentrifugation in a Beckman TLA 100.2 rotor for 10 min at 50,000 rpm (Beckman Instruments, Palo Alto, CA). The supernatant was dialyzed (Spectra-Por No. 7 tubing 50,000 MW cut-off) overnight at 4°C against 200 ml of 25 mM HEPES buffer (pH 8.0) containing 1 mM EDTA, 1 mM β-mercaptoethanol, and 4.2 mM DHPC. The ~1.5 ml solution was then subjected to anion exchange FPLC using a Pharmacia (Uppsala, Sweden) Resource Q column with a linear NaCl gradient. Fractions (0.5 ml) were collected using a Pharmacia AKTA system.

Electron microscopy and image analysis

Aliquots (~4 μl) were allowed to adhere for ~90 s to carbon-coated copper grids that had been rendered hydrophilic by glow discharge in an atmosphere of amylamine and then stained with 2% uranyl acetate (Ted Pella, Tustin, CA). Images were recorded under minimum electron dose conditions using a CM120 electron microscope (Philips Electron Optics/FEI, Eindhoven, The Netherlands). An optical diffractometer was used to select micrographs that showed minimal astigmatism and drift.

Images were recorded on Kodak SO163 film at a nominal magnification of 45,000 using 100 kV electrons. Micrographs were digitized with a SCAI scanner (Carl Zeiss, Oberkochen, Switzerland) at 8 bits per pixel and 7 μm per pixel, subsequently averaged to 14 μm per pixel. The optical density for each negative was adjusted to give a mean value of ~127 over the total range

of 0–255. Image processing was carried out with the EMAN suite (see (43)). Visual inspection showed a few particles that appeared to have fourfold symmetry. Twenty-three of these particles were manually selected and aligned and averaged using a reference-free algorithm. The averaged particle was then used as a reference for initial particle selection. Six negatives were screened by a cross-correlation method in the EMAN program boxer, yielding 2,148 particles. Initial models were generated using the EMAN routine *startcsym*, which conducts a symmetry search of the particles for fourfold and mirror symmetry, representing top and side views, respectively. These orthogonal projections are subsequently aligned with a common-lines algorithm and back-projected to generate a 3D structure. Different models were generated with different particle sets. The models had a similar overall shape and dimensions, but only correlated to ~75% at 100 Å and fell to ~0% correlation at 40 Å (see Fig. 4 *b*). Models were subjected to refinement with imposed C4 symmetry using an angular increment of 5°. The refinement converged to the final model as judged by Fourier shell correlation comparisons between solutions with different starting models. The isosurface for the final model was determined from the molecular mass of the tetramer (384 kDa) that encloses a volume of 470,000 $Å^3$ using a protein partial specific volume of 0.74 cm^3/g. Atomic coordinates for Kv1.2 were visually fitted within the EM map.

RESULTS

Electron microscopy and strategy for image reconstruction of Kv2.1

Human Kv2.1 was expressed in a stably transfected line of CHO cells (29), and isolated membranes were solubilized in DHPC. Anion exchange chromatography provided substantial purification (Fig. 2). Electron micrographs of negatively stained, detergent-solubilized protein showed compact particles that were selected by an automated cross-correlation method with projections generated from a crude, preliminary model (Fig. 3). This approach minimized bias compared with manual selection by visual inspection; 6,382 individual particles were selected and subjected to multiple refinements starting with two different models. This approach reduced initial model bias during the reconstruction and allowed a more accurate assessment of the final resolution. Although particles occur on the grid in all orientations, there was a marked preference for orientations in which the long axis was parallel with the carbon surface (Fig. 4 *a*), which also occurred with detergent-solubilized *Shaker* channels (15).

The contrast transfer function (CTF) of the electron microscope modulates the amplitude and phase information in the images (34). In using the EMAN software package for image reconstruction, we corrected for phase effects but not amplitude effects due to the CTF. The contrast produced by negative stain is pronounced at low spatial frequencies, and the additional envelope function contrast compensates for amplitude suppression by the CTF. As noted by Erickson and Klug (34) the CTF of negatively stained specimens is dominated by amplitude contrast, rather than phase contrast, as in electron cryomicroscopy (cryoEm). In negative stain, the amplitudes at low spatial frequencies are boosted compared with frequencies beyond ~30 $Å^{-1}$. In the circularly averaged power spectrum of the Kv2.1 particles, the amplitudes between 120–

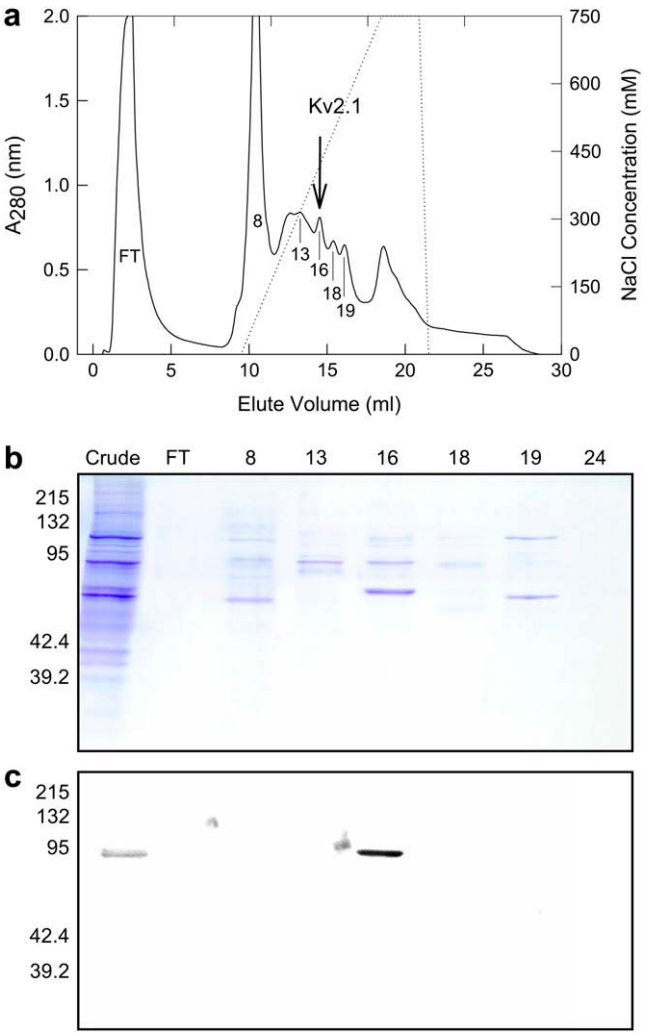

FIGURE 2 Purification of Kv2.1 channels. (*a*) Chromatogram of anion-exchange purification of DHPC-solubilized Kv2.1 from CHO cells. Solid line corresponds to absorbance of eluate at 280 nm. Dashed line corresponds to NaCl concentration of elution buffer. FT (flow through) and specific fractions (8,13,16,18,19,24) are indicated. (*b*) Coomassie-stained SDS-gel of crude CHO cell membranes expressing Kv2.1 and specific column fractions indicated in (*a*). (*c*) Western immunoblot generated using polyclonal rabbit antibodies directed against the amino acid sequence CHMLPGGGAHGS-TRDQSI in Kv2.1. Only crude membranes and fraction 16 showed signal for Kv2.1.

50 $Å^{-1}$ dominated the power spectrum, and artifacts would be generated if these amplitudes are further boosted. In addition, there are reports of suspect results obtained with EMAN when CTF amplitudes are applied iteratively throughout the refinement. For instance, in a cryoEM study of GroEL (35), Stagg et al. carried out reconstructions with and without CTF amplitude corrections. Although the nominal resolution for the latter reconstruction was greater (as estimated by the Fourier shell correlation method), the actual features of the two maps were nearly identical. These authors concluded that applying CTF amplitude corrections during a refinement generated

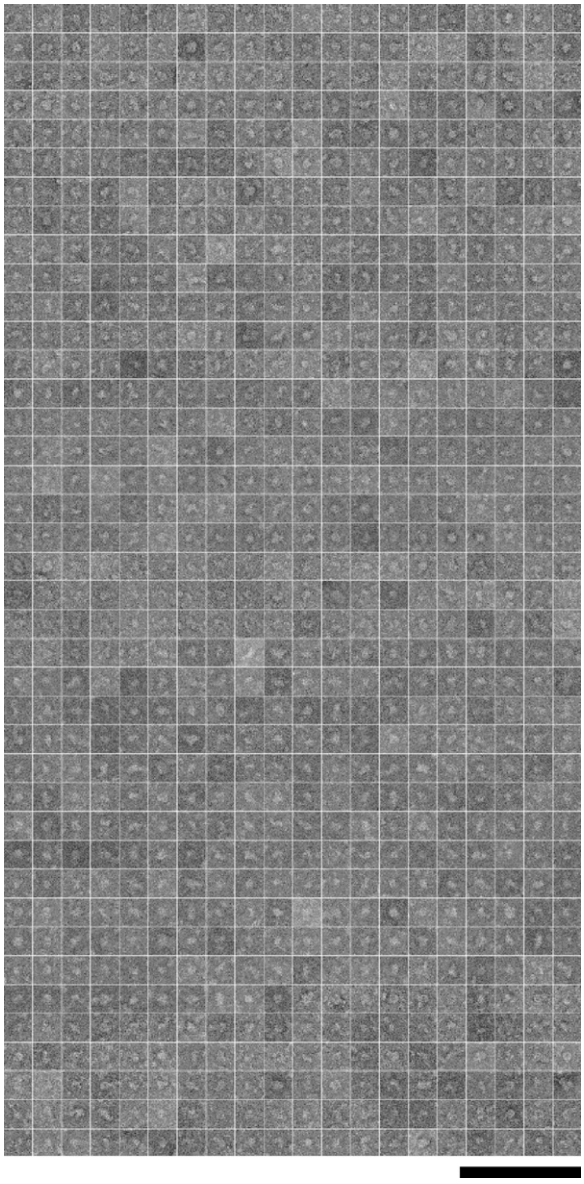

FIGURE 3 Gallery of raw particle images of negatively stained Kv2.1 selected from several electron micrographs. Perusal of the images and comparison with the 3D reconstruction (Fig. 5) suggest that there is a preference for the particles to lie with their long axis parallel to the plane of the carbon film of the EM grid. Scale bar, 500 Å.

maps with greater correlated noise, producing FSC results that are not reliable. Consequently, we only corrected for the phase component of the CTF.

We realize that model bias will greatly influence the averaging of multiple conformations of a single molecule. The EMAN algorithm contains a randomization factor, to modify the order in which particles are selected for alignment and averaging, in the generation of class averages. Underlying noise in the data influences small data sets unpredictably, and averages will tend to ''wander'' somewhat due to noise. We believe that the use of multiple models is thus a more reliable measure of which features are actually present in the macromolecular complex. For this reason we used two different starting models and derived independent 3D reconstructions.

To estimate the resolution of a 3D reconstruction, a common approach is to split the data set in half, compute two maps using the particle orientations from the final round of refinement, and compare the correlation coefficient between the two maps in resolution shells in reciprocal space. A typical cut-of value is the resolution corresponding to a correlation coefficient of 0.5. By this approach, the resolution was estimated as 19 Å for each of the two starting models (Fig. 4 *b*). The concern we have with the conventional split method is that all of the particle images have already been classified with a single model, which biases the results. For this reason, we also generated a correlation coefficient profile in which we compared the final maps derived from different starting models. (Although similar in general shape, the starting models used for the refinements were quite different as the initial maps correlated only to ~75% at 100 Å resolution, and to ~0% at 40 Å (Fig. 4 *b*)). By a similar Fourier shell correlation method, the final two maps derived from different starting models had a resolution of 25 Å at the 0.5 cut-off value. We suspect that the extended resolution of 19 Å calculated by splitting the data set may be an artifact due to correlation of noise. Consequently, the maps displayed in Figs. 5–9 were computed at the more conservative resolution of 25 Å.

Structure of Kv2.1 at 25 Å resolution

Fourfold rotational symmetry imposed during the processing yielded a roughly egg-shaped complex with a long axis of ~120 Å and a diameter of ~80 Å at the widest section (Fig. 5, *a* and *b*). A distinctive feature are four L-shaped arms of density that extend the length of the molecule, bent at ~45° with respect to the axis of the channel (Fig. 5, *d* and *e*). At an isosurface level that encloses the expected volume of the tetrameric complex (~470,000 $Å^3$), all internal vestibules are completely enclosed, with no windows to the cytoplasmic space. Also, the interior of the protein is entirely filled with density, with the exception of a small chamber in the narrower half of the molecule (Figs. 5 *c* and 6, *e* and *g*). The density within the narrower half of the molecule is more diffuse, and at a lower isosurface level another chamber is found immediately above the first in the center of the channel (Figs. 5 *f* and 6 *c*). At this isosurface level, small windows appear in the center of the complex (Fig. 5, *d* and *e*).

Fit of the Kv1.2 x-ray structure into the Kv2.1 map

The TM assembly of Kv1.2 fits very well within the wider section of the Kv2.1 map (Fig. 7). The four upper arms on the perimeter of the Kv2.1 map correspond to the S2 and S3

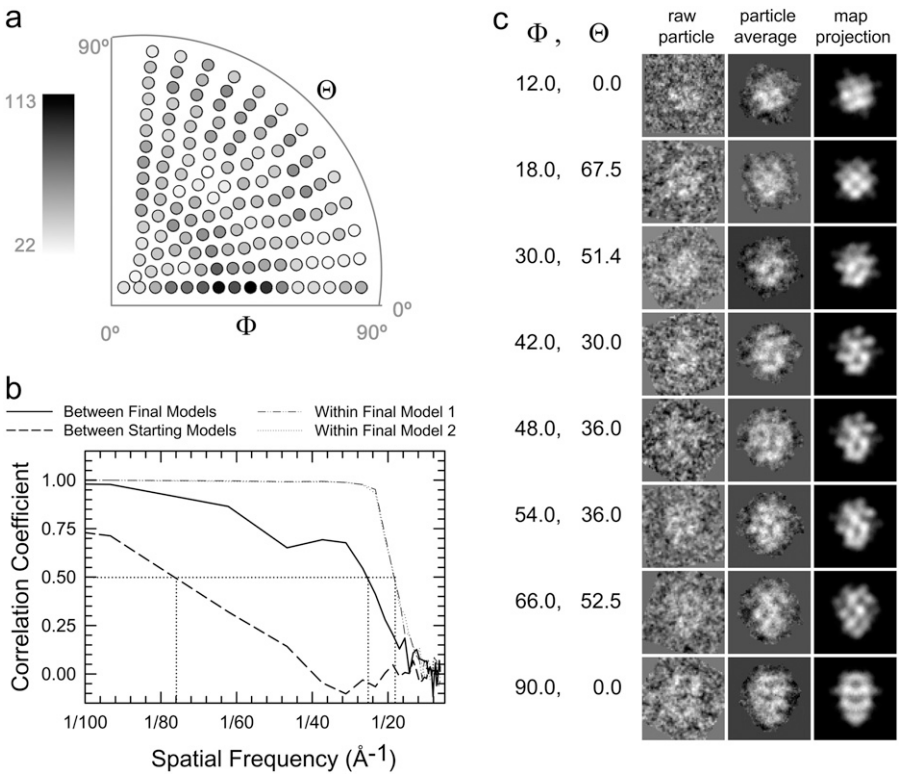

FIGURE 4 Single particle image analysis. (*a*) Histogram displaying the classification of the individual particles from the final round of refinement. Each spot represents a particular orientation of the two Euler angles Φ and Θ, and is assigned a grayscale value based on the number of particles assigned to that orientation. White represents 0 particles, and black the maximum of 113 particles. (*b*) Fourier shell correlation between two maps each calculated from the full data set but with different starting maps (*solid line*). The correlation drops below 0.5 at ~25 Å resolution. For comparison, the correlation between the starting maps is also shown (*dashed line*). Also displayed are Fourier shell correlations for the final maps created with the first (*dotted line*) and second (*dotted-dashed line*) starting models. The graph shows correlations between maps generated by splitting the data set and calculating two maps using the Euler angle assignments from the final round of refinement. The two plots are very similar, with a 0.5 correlation at ~19 Å for both. For convenience, horizontal and vertical dotted lines have been added at the 0.5 correlation level to indicate the resolution for each of the curves. (*c*) Representative particles from different orientations. The left column contains examples of raw particles assigned to a given orientation. The middle column contains images generated by averaging all the raw particles in the orientation group. The images in the right column are generated by projecting the final 3D map at the indicated orientation.

helices, and the elbow of density between the upper and lower arms corresponds to the T1 linker–S1 junction in Kv1.2 (Fig. 7 *c*). These features dictate the rotational register of Kv1.2 within the Kv2.1 map. Only the S3–S4 junction projects beyond the Kv2.1 map envelope. In the Kv1.2 crystal structure, this loop forms a crystal contact with the β-subunit from a neighboring molecule (6). In addition, the S3–S4 helical assembly seems to be only loosely packed

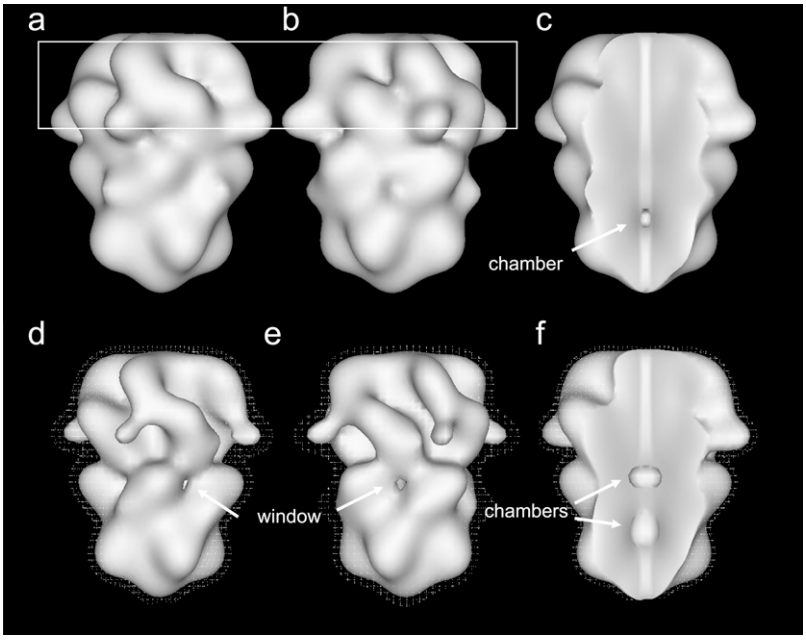

FIGURE 5 Surface-shaded, 3D density map of human Kv2.1 at ~25 Å resolution. The fourfold axis is oriented in the *y* direction. The maps have been aligned such that the putative cytoplasmic and TM domains are oriented at the bottom and top, respectively. (*a*) View with the isosurface contour set to include the expected volume for the entire tetrameric complex. (*b*) The same map as (*a*) but rotated by 45° around the fourfold axis. The white lines are spaced at 30 Å and indicate the presumed location of the lipid bilayer. (*c*) The same view as *a* but with a sagittal section removed to show an interior chamber at this isosurface level. (*d* and *e*) The same views as *a* and *b*, respectively, but with a contour set to a lower level that includes only 66% of the expected volume to visualize windows into the internal space. The white mesh represents the expected isosurface for the full protein. (*f*) A sagittal section at a lower (75%) isosurface level to display an additional internal chamber.

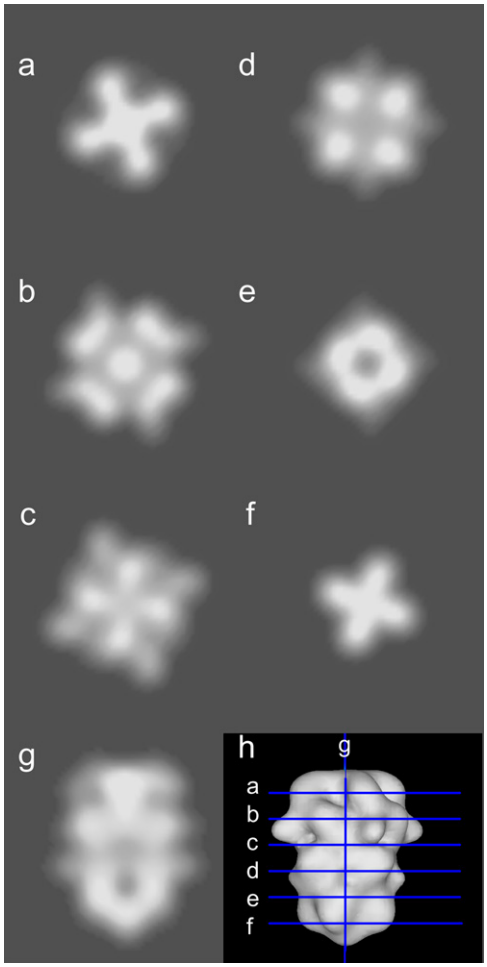

FIGURE 6 Coronal sections of density (*a–f*) and a sagittal section (*g*) through the 3D map of Kv2.1 are shown in grayscale, in which white is the highest density (corresponding to protein). The surface-shaded view of the 3D map (*h*) provides a key indicating the position of the slices in the map.

against the rest of the molecule. It is possible that crystal packing in Kv1.2 has distorted the S3–S4 assembly, and in solution, the structure would actually be enclosed within the Kv2.1 map. At the highest isosurface contour levels, the dense, central structure centered on the fourfold axis is a prominent feature (Fig. 8). There is a good fit of the KcsA x-ray structure to this density (Fig. 8), which corresponds to the four S5-P-S6 sequences in Kv2.1.

The position of the Kv1.2 structure within the Kv2.1 map places the T1 domain within the lower, narrower section of the map (Fig. 7 *a*). A small chamber is noted directly at the bottom of the T1 domain (Fig. 8). T1 is otherwise surrounded by density not otherwise accounted for, which we assign to the C-terminal domains. For instance, the lower arms of density at the sides of the narrower half of the molecule (Fig. 5) are presumably portions of the C-terminus that embrace the surface of T1. At higher isosurface levels, an additional chamber is found immediately above T1 (Figs. 5 *f* and 8).

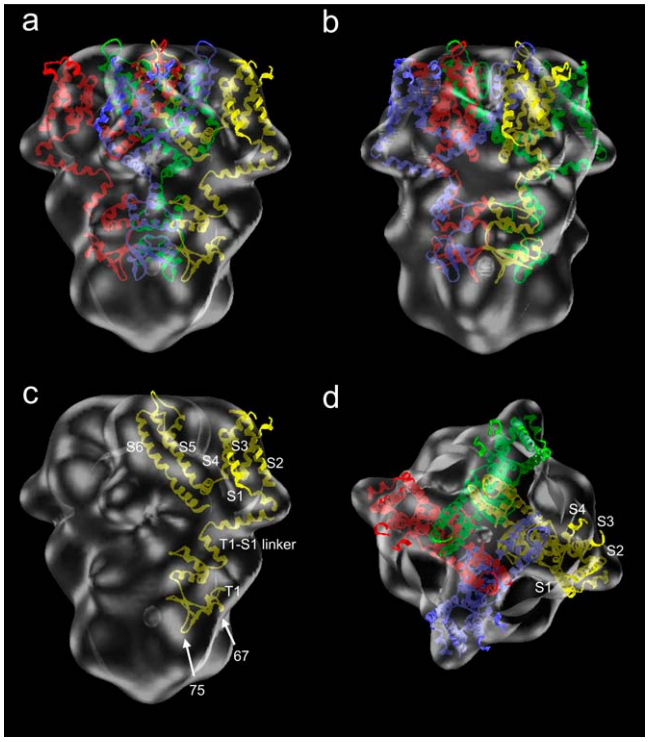

FIGURE 7 Fit of the x-ray crystal structure of Kv1.2 into the Kv2.1 map. The views in *a* and *b* are related by a 45° rotation about the fourfold axis. The isosurface for the Kv2.1 map has been set to include 100% of the expected protein volume. The four polypeptide chains have been given different colors. Gaps in the Kv1.2 ribbon trace result from an incomplete chain trace in the Kv1.2 pdb file (5). (*c*) The same view in *a* but only a single Kv1.2 subunit is displayed. The T1 domain and TM helices have been labeled. Also indicated are the predicted positions of residues 67 and 75, which are believed to interact with the C-terminal domains. (*d*) View of the fit rotated with the fourfold symmetry axis pointing toward the viewer.

DISCUSSION

A number of studies by negative-stain electron microscopy and single particle image analysis have been conducted for voltage-gated K^+ channels: *Shaker* (14,15), Kv1.x (16), Kv1.2 (17), and Kv4.2 (36). Our study of Kv2.1 is the first to derive a 3D map of a K^+ channel in the Kv2.x family.

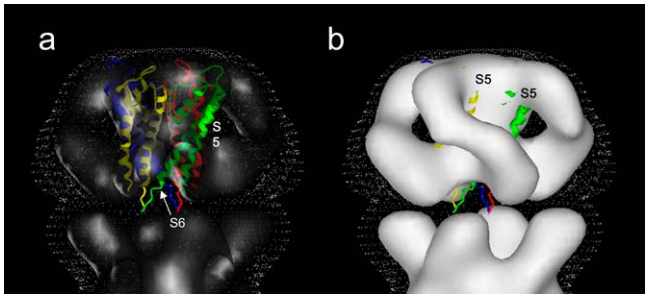

FIGURE 8 Fit of KcsA into the transmembrane region of the Kv2.1 map. The isosurface has been set to 33% of the expected volume. Close-ups with transparent (*a*) and solid (*b*) Kv2.1 maps.

In all the previous low resolution EM maps, the T1 and TM assemblies were readily distinguishable, forming distinct rings, with the smaller ring assigned to the ''hanging gondola'' of T1. The hanging gondola is not apparent in Kv2.1, which instead possesses a large cytoplasmic domain defined by continuous density throughout, such that the expected position of T1 is completely enclosed (Figs. 5 *f*, 7 *a*, and 9). This continuous shell of density is generated when the map is contoured at a level to contain the expected mass of the protein. At higher isosurface levels, there are small windows between the putative T1 and TM assemblies (Fig. 5, *d* and *e*).

We have been careful not to over interpret the density variation in the map. At an isosurface value that encloses 100% of the expected volume, the surface of the protein is contiguous, no windows are seen, there is little internal detail, and only a very small internal chamber is visible. The interest in the windows is due to the fact that they are prominent in every other Kv structure solved to date, and are widely believed to be the pathway for K^+ entry into the pore. For example, *Shaker* (15) and Kv4.2 (36) possess very large windows between the two domains, although mammalian Kv1 has much smaller, but still visible, windows (16). In *Shaker*, only a single N-terminal inactivation domain is required to block the channel (37), which is believed to snake in through the windows in the side to block the channel (38). The lack of this conserved and necessary feature in the map of Kv2.1 requires some explanation. The appearance of windows at lower contour levels is in concordance with the architecture of other Kv channels. The windows that do appear are reproducibly seen in the independent reconstructions from both starting models. For these reasons we believe that

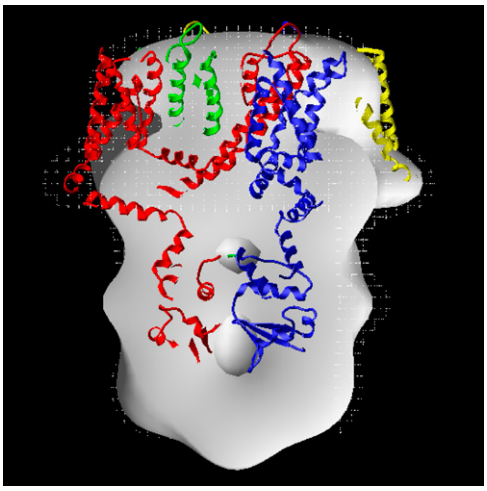

FIGURE 9 Kv2.1 map with the fit Kv1.2 structure. The alignment of the transmembrane domains of the Kv1.2 structure within the Kv2.1 map places the Kv1.2 T1 domain within a region of high density in the Kv2.1 map. Surrounding regions of lower density are ascribed to putative aqueous chambers. The map density has been cut away to allow visualization of the T1 domain relative to the internal spaces. The map isosurface is set at 80% so that the upper and lower chambers can be visualized. The chambers appear both above and below T1.

K^+ permeation does indeed proceed through openings in the sides of the channel, but the windows are smaller when compared with other Kv channels. However, it is difficult to estimate the size of the windows. Uranyl acetate granules have a diameter of ~15 Å, so any window with a smaller size would exclude stain and not be detected. In addition, stain penetration might be impeded by negative charges clustered at the openings. In this case, the windows could be larger than 15 Å and still be identified as continuous density in the map. The upper size limit of 15 Å provided by the stain is certainly large enough to allow entry of hydrated K^+ ions, as well as a single polypeptide chain, as is proposed for N-terminal inactivation. As is true of other Kv channels, the N-terminus of Kv2.1 is known to inactivate when added in trans (39), which argues against a conformation in which the windows are too small to allow peptide entry.

Differences in the cytoplasmic domains of Kv2.1 and *Shaker* may be accounted for by the C-terminal domains. Kv2.1 possesses a much larger C-terminal domain than does *Shaker*: ~17 kDa/subunit in *Shaker* vs. ~46 kDa/subunit in Kv2.1 (Fig. 1). They must begin at the central interior, at the ends of S6. As such, they might contribute to the density between the expected position of T1 and the TM domains (Figs. 7 and 9). In addition, at least part of the arms that embrace the T1 domain may be composed of the C-termini, so that much of the extra protein may well be enclosing the distal end of the T1 domain in Kv2.1.

There is evidence that the C-terminal domains of Kv2.1 interact with each other. In contrast with Kv1.1, where the N-terminal domains are required for tetramerization (40), Kv2.1 is able to form channels when the T1 domain has been deleted, although these channels have greatly altered activation kinetics (41). In addition, soluble fragments of the Kv2.1 C-terminus coexpressed with the full-length protein in *Xenopus* oocytes (42) act as a dominant negative suppressor of channel conductance.

In addition to interactions between the C-termini, a recent study using mutagenesis and cross-linking (24) suggests that there is a direct interaction between the N- and C-terminal domains of Kv2.1. Human and rat Kv2.1 display different activation rates, and mutational studies of recombinant Kv2.1 chimera identified two residues (67 and 75) in T1 and two regions (749–795 and 796–838) at the end of the C-terminus responsible for this effect (24). Residues 67 and 75 lie near the distal surface of T1 in homology models (Fig. 7 *c*), but direct interaction between these residues and the end of the C-terminal domain is possible in the Kv2.1 map, where there is extra volume at the side of T1 to accommodate the C-terminus. Difference EM maps with C-terminally truncated *Shaker* indicated that the C-terminus extends to the sides of T1 (14), consistent with our assignment of the L-shaped arms in Kv2.1 to the C-terminal density.

Additional experiments with Kv2.1/Kv1.2 chimerae suggest that gating effects are communicated by direct connection between the cytoplasmic domains and the S4–S5 linker (25).

In the Kv2.1 map, there is certainly contiguous density between the S4–S5 linker and the cytoplasmic density (Figs. 7 *c* and 9), suggesting physical continuity between these domains in Kv2.1. Channel gating seems to be associated with physical movements of the C-termini (26) as determined by fluorescence resonance energy transfer. Labels were attached at the N- and C-termini of Kv2.1, and there was a relatively large movement (10–20 Å) in the plane of the membrane associated with channel gating.

The central core of the membrane spanning region in Kv2.1 forms a dense (stain-excluding) structure running along the fourfold axis, extending the full length of the membrane (Figs. 5, *c* and *f*, and 6, *a* and *b*). The simplest interpretation is that this represents protein density corresponding to a closed conformation of the channel. In the x-ray structure of KcsA, the S5 and S6 helices form a cone-shaped structure above the selectivity filter. In KcsA, four pairs of antiparallel α-helices approach one another at the vertex of the cone (Fig. 8 *a*). This configuration prevents access by K^+ ions to the channel formed by the selectivity filter, implying that KcsA crystallizes in the closed form. In contrast, the vertex is more open in Kv1.2 and very open in KvAP, implying that these structures are in open conformations. The central core of the transmembrane assembly in the Kv2.1 map provides a good fit for S5 and S6 (Fig. 8) from KcsA, suggesting that Kv2.1 may indeed be in a closed form.

Although the width of the TM assembly (75–85 Å) is smaller than that of mammalian Kv1.x (125 Å (16)), *Shaker* (100 Å (15)), or Kv4.2 (115 Å (36)), the TM domain is fit quite well with the Kv1.2 structure (Fig. 7). In particular, the elbows of density at the edges of the TM domain of the EM map are fit very well with the T1 linker–S1 connecting loop. At an isosurface enclosing 100% of the expected Kv2.1 mass, all of the TM domains in Kv1.2 are enclosed within the map density, with the exception of the ends of S3–S4 at the extracellular side (Fig. 7 *c*).

Our study provides the first view of a Kv2x class of K^+ channels in which there is close correspondence in the molecular design of the transmembrane assembly and T1 domains. Substantial additional density is closely associated with T1 and is ascribed to the ~184 kDa C-terminal regulatory domains within each tetramer.

We thank Michael E. Pique for assistance with figure preparation.

This work was supported by National Institutes of Health grants RO1 HL48908 (M.Y.) and RO1 DK048494 (L.P.), American Heart Association Grant-in-Aid (M.Y.), National Institutes of Health training grant AI-07354 (B.D.A.), and a Wayne Green Fellowship in Cardiovascular Medicine (B.D.A.). During part of this work, M.Y. was the recipient of a Clinical Scientist Award in Translational Research from the Burroughs Wellcome Fund.

REFERENCES

1. Minor, D. L., Jr. 2001. Potassium channels: Life in the post-structural world. *Curr. Opin. Struct. Biol.* 11:408–414.
2. Yellen, G. 2002. The voltage-gated potassium channels and their relatives. *Nature*. 419:35–42.
3. Doyle, D. A., J. Morais Cabral, R. A. Pfuetzner, A. Kuo, J. M. Gulbis, S. L. Cohen, B. T. Chait, and R. MacKinnon. 1998. The structure of the potassium channel: Molecular basis of K^+ conduction and selectivity. *Science*. 280:69–77.
4. Zhou, Y., J. H. Morais-Cabral, A. Kaufman, and R. MacKinnon. 2001. Chemistry of ion coordination and hydration revealed by a K^+ channel-Fab complex at 2.0 Å resolution. *Nature*. 414:43–48.
5. Jiang, Y., A. Lee, J. Chen, V. Ruta, M. Cadene, B. T. Chait, and R. MacKinnon. 2003. X-ray structure of a voltage-dependent K^+ channel. *Nature*. 423:33–41.
6. Long, S. B., E. B. Campbell, and R. Mackinnon. 2005. Crystal structure of a mammalian voltage-dependent Shaker family K^+ channel. *Science*. 309:897–903.
7. Long, S. B., E. B. Campbell, and R. Mackinnon. 2005. Voltage sensor of Kv1.2: Structural basis of electromechanical coupling. *Science*. 309: 903–908.
8. Jiang, Y., V. Ruta, J. Chen, A. Lee, and R. MacKinnon. 2003. The principle of gating charge movement in a voltage-dependent K^+ channel. *Nature*. 423:42–48.
9. Cha, A., G. E. Snyder, P. R. Selvin, and F. Bezanilla. 1999. Atomic scale movement of the voltage-sensing region in a potassium channel measured via spectroscopy. *Nature*. 402:809–813.
10. Bezanilla, F. 2002. Voltage sensor movements. *J. Gen. Physiol.* 120: 465–473.
11. Gandhi, C. S., and E. Y. Isacoff. 2002. Molecular models of voltage sensing. *J. Gen. Physiol.* 120:455–463.
12. Horn, R. 2002. Coupled movements in voltage-gated ion channels. *J. Gen. Physiol.* 120:449–453.
13. Kreusch, A., P. J. Pfaffinger, C. F. Stevens, and S. Choe. 1998. Crystal structure of the tetramerization domain of the Shaker potassium channel. *Nature*. 392:945–948.
14. Sokolova, O., A. Accardi, D. Gutierrez, A. Lau, M. Rigney, and N. Grigorieff. 2003. Conformational changes in the C terminus of *Shaker* K^+ channel bound to the rat Kvβ2-subunit. *Proc. Natl. Acad. Sci. USA*. 100:12607–12612.
15. Sokolova, O., L. Kolmakova-Partensky, and N. Grigorieff. 2001. Three-dimensional structure of a voltage-gated potassium channel at 2.5 nm resolution. *Structure*. 9:215–220.
16. Orlova, E. V., M. Papakosta, F. P. Booy, M. van Heel, and J. O. Dolly. 2003. Voltage-gated K^+ channel from mammalian brain: 3D structure at 18 Å of the complete $\alpha_4\beta_4$ complex. *J. Mol. Biol.* 326:1005–1012.
17. Parcej, D. N., and L. Eckhardt-Strelau. 2003. Structural characterisation of neuronal voltage-sensitive K^+ channels heterologously expressed in *Pichia pastoris*. *J. Mol. Biol.* 333:103–116.
18. Surmeier, D. J., and R. Foehring. 2004. A mechanism for homeostatic plasticity. *Nat. Neurosci.* 7:691–692.
19. Park, K.-S., D. P. Mohapatra, H. Misonou, and J. S. Trimmer. 2006. Graded regulation of the Kv2.1 potassium channel by variable phosphorylation. *Science*. 313:976–979.
20. Du, J., L. L. Haak, E. Phillips-Tansey, J. T. Russell, and C. J. McBain. 2000. Frequency-dependent regulation of rat hippocampal somatodendritic excitability by the K^+ channel subunit Kv2.1. *J. Physiol.* 522:19–31.
21. Wray, D. 2004. The roles of intracellular regions in the activation of voltage-dependent potassium channels. *Eur. Biophys. J.* 33:194–200.
22. Misonou, H., D. P. Mohapatra, E. W. Park, V. Leung, D. Zhen, K. Misonou, A. E. Anderson, and J. S. Trimmer. 2004. Regulation of ion channel localization and phosphorylation by neuronal activity. *Nat. Neurosci.* 7:711–718.
23. Mohapatra, D. P., and J. S. Trimmer. 2006. The Kv2.1 C terminus can autonomously transfer Kv2.1-like phosphorylation-dependent localization, voltage-dependent gating, and muscarinic modulation to diverse Kv channels. *J. Neurosci.* 26:685–695.

24. Ju, M., L. Stevens, E. Leadbitter, and D. Wray. 2003. The Roles of N- and C-terminal determinants in the activation of the Kv2.1 potassium channel. *J. Biol. Chem.* 278:12769–12778.

25. Scholle, A., T. Zimmer, R. Koopmann, B. Engeland, O. Pongs, and K. Benndorf. 2004. Effects of Kv1.2 intracellular regions on activation of Kv2.1 channels. *Biophys. J.* 87:873–882.

26. Kobrinsky, E., L. Stevens, Y. Kazmi, D. Wray, and N. M. Soldatov. 2006. Molecular rearrangements of the Kv2.1 potassium channel termini associated with voltage gating. *J. Biol. Chem.* 281:19233–19240.

27. Henquin, J.-C. 2000. Triggering and amplifying pathways of regulation of insulin secretion by glucose. *Diabetes.* 49:1751–1760.

28. Herrington, J. 2007. Gating modifier peptides as probes of pancreatic β-cell physiology. *Toxicon.* 49:231–238.

29. Roe, M. W., J. F. Worley 3rd, A. A. Mittal, A. Kuznetsov, S. DasGupta, R. J. Mertz, S. M. Witherspoon 3rd, N. Blair, M. E. Lancaster, M. S. McIntyre, W. R. Shehee, I. D. Dukes, and L. H. Philipson. 1996. Expression and function of pancreatic β-cell delayed rectifier K^+ channels. Role in stimulus-secretion coupling. *J. Biol. Chem.* 271: 32241–32246.

30. MacDonald, P. E., X. F. Ha, J. Wang, S. R. Smukler, A. M. Sun, H. Y. Gaisano, A. M. Salapatek, P. H. Backx, and M. B. Wheeler. 2001. Members of the Kv1 and Kv2 voltage-dependent K^+ channel families regulate insulin secretion. *Mol. Endocrinol.* 15:1423–1435.

31. MacDonald, P. E., S. Sewing, J. Wang, J. W. Joseph, S. R. Smukler, G. Sakellaropoulos, J. Wang, M. C. Saleh, C. B. Chan, R. G. Tsushima, A. M. F. Salapatek, and M. B. Wheeler. 2002. Inhibition of Kv2.1 voltage-dependent K^+ channels in pancreatic β-cells enhances glucose-dependent insulin secretion. *J. Biol. Chem.* 277:44938–44945.

32. Tamarina, N. A., A. Kuznetsov, L. E. Fridlyand, and L. H. Philipson. 2005. Delayed-rectifier (Kv2.1) regulation of pancreatic β-cell calcium responses to glucose: Inhibitor specificity and modeling. *Am. J. Physiol.* 289:E578–E585.

33. Herrington, J., Y.-P. Zhou, R. M. Bugianesi, P. M. Dulski, Y. Feng, V. A. Warren, M. M. Smith, M. G. Kohler, V. M. Garsky, M. Sanchez, M. Wagner, K. Raphaelli, P. Banerjee, C. Ahaghotu, D. Wunderler, B. T. Priest, J. T. Mehl, M. L. Garcia, O. B. McManus, G. J. Kaczorowski, and R. S. Slaughter. 2006. Blockers of the delayed-rectifier potassium current in pancreatic β-cells enhance glucose-dependent insulin secretion. *Diabetes.* 55:1034–1042.

34. Erickson, H. P., and A. Klug. 1971. Measurement and compensation of defocusing and aberrations by Fourier processing of electron micrographs. *Philos. Trans. R. Soc. Lond., B, Biol. Sci.* 261:105–118.

35. Stagg, S. M., G. C. Lander, J. Pulokas, D. Fellmann, A. Cheng, J. D. Quispe, S. P. Mallick, R. M. Avila, B. Carragher, and C. S. Potter. 2006. Automated cryoEM data acquisition and analysis of 284742 particles of GroEL. *J. Struct. Biol.* 155:470–481.

36. Kim, L. A., J. Furst, D. Gutierrez, M. H. Butler, S. Xu, S. A. Goldstein, and N. Grigorieff. 2004. Three-dimensional structure of I_{to}; Kv4.2-KChIP2 ion channels by electron microscopy at 21 Angstrom resolution. *Neuron.* 41:513–519.

37. MacKinnon, R., R. W. Aldrich, and A. W. Lee. 1993. Functional stoichiometry of Shaker potassium channel inactivation. *Science.* 262: 757–759.

38. Zhou, M., J. H. Morais-Cabral, S. Mann, and R. MacKinnon. 2001. Potassium channel receptor site for the inactivation gate and quaternary amine inhibitors. *Nature.* 411:657–661.

39. Gebauer, M., D. Isbrandt, K. Sauter, B. Callsen, A. Nolting, O. Pongs, and R. Bähring. 2004. N-type inactivation features of Kv4.2 channel gating. *Biophys. J.* 86:210–223.

40. Shen, N. V., X. Chen, M. M. Boyer, and P. J. Pfaffinger. 1993. Deletion analysis of K^+ channel assembly. *Neuron.* 11:67–76.

41. VanDongen, A. M. J., G. C. Frech, J. A. Drewe, R. H. Joho, and A. M. Brown. 1990. Alteration and restoration of K^+ channel function by deletions at the N- and C-termini. *Neuron.* 5:433–443.

42. Bentley, G. N., M. A. Brooks, C. A. O'Neill, and J. B. C. Findlay. 1999. Determinants of potassium channel assembly localised within the cytoplasmic C-terminal domain of Kv2.1. *Biochim. Biophys. Acta.* 1418:176–184.

43. Ludtke, S. J., P. R. Baldwin, and W. Chiu. 1999. EMAN: semi-automated software for high-resolution single-particle reconstructions. *J. Struct. Biol.* 128:82–97.

44. Thompson, J. D., D. G. Higgins, and T. J. Gibson. 1994. CLUSTAL W: improving the sensitivity of progressive multiple sequence alignment through sequence weighting, position-specific gap penalties and weight matrix choice. *Nucleic Acids Res.* 22:4673–4680.